Liquid-like assembly of VASP drives actin polymerization and bundling

Authors:

Kristin Graham[1], Aravind Chandrasekaran[2], Liping Wang[3], Aly Ladak[1], Eileen M. Lafer[3], Padmini Rangamani[2*], Jeanne C. Stachowiak[1*]

[1] *University of Texas at Austin, Department of Biomedical Engineering*

[2] *University of California San Diego, Department of Mechanical and Aerospace Engineering*

[3] *University of Texas Health Science Center at San Antonio, Department of Biochemistry and Structural Biology*

To whom correspondence should be addressed: padmini.rangamani@eng.ucsd.edu, jcstach@austin.utexas.edu

ABSTRACT

The organization of actin filaments into bundles is required for cellular processes such as motility, morphogenesis, and cell division. Filament bundling is controlled by a network of actin binding proteins. Recently, several proteins that comprise this network have been found to undergo liquid-liquid phase separation. How might liquid-like condensates contribute to filament bundling? Here we show that the processive actin polymerase, VASP, forms liquid-like droplets under physiological conditions. As actin polymerizes within VASP droplets, elongating filaments partition to the edges of the droplet to minimize filament curvature, forming an actin-rich ring within the droplet. The rigidity of this ring is balanced by the droplet's surface tension, as predicted by a continuum-scale computational model. However, as the ring grows thicker, its rigidity increases and eventually overcomes the surface tension of the droplet, deforming into a linear bundle. The resulting bundles contain parallel actin filaments that grow from their tips. Growing bundles zipper together upon contact with one another, an effect which is mediated by the surface tension of the liquid-like VASP droplets that encapsulate them. Once the parallel arrangement of filaments is created within a VASP droplet, it propagates through the addition of new actin monomers to achieve a length that is many times greater than the initial droplet. This droplet-based mechanism of bundling may be relevant to the assembly of cellular architectures rich in parallel actin filaments, such as filopodia, stress fibers, and focal adhesions.

INTRODUCTION

VASP is an actin filament nucleator and polymerase that catalyzes the processive elongation of actin filaments at the leading edge of cells, in focal adhesions, and at filopodial tips [1]. VASP plays a significant role in cell motility, adhesion, and sensing. It is part of the Ena/VASP family of proteins that share a conserved modular structure. In particular, VASP exists as a homo-tetramer, where each monomer consists of an N-terminal EVH1 domain, a central proline rich region, and a C-terminal EVH2 domain [2].

The EVH1 domain is a conserved domain that allows for localization of VASP to the plasma membrane by binding to specific proline-rich motifs in lamellipodin, vinculin, and zyxin, among others [3-6]. The central proline-rich region mediates binding to other cytoskeletal proteins such as profilin, as well as SH3-containing proteins such as the membrane scaffolding protein, IRSp53 [7, 8]. The C-terminal, WH2-like EVH2 domain consists of G-actin and F-actin binding domains, which together confer the polymerase activity of VASP, as well as a coiled-coil domain that mediates tetramerization [9, 10].

The capacity of the VASP tetramer to form multivalent networks with other actin-binding proteins suggests that it could provide a scaffold for assembly of protein networks. Indeed, VASP has been found to form dynamic protein assemblies both *in vivo* and *in vitro*. The proteins IRSp53 and lamellipodin have both been shown to recruit VASP to the plasma membrane, forming dynamic protein-rich clusters [7, 11]. These clusters can function to localize actin polymerization and, in some cases, precede filopodia formation. VASP has also been found to cluster on actin filaments with lamellipodin [12]. These assemblies of VASP are thought to be critical for the processive elongation of actin filaments, as clustering of VASP results in more robust actin polymerization [13, 14]. Collectively, these studies suggest that protein assemblies rich in VASP help to organize the cytoskeleton in multiple cellular contexts.

Increasing evidence suggests that many cellular proteins are organized into liquid-like condensates through the process of liquid-liquid phase separation (LLPS) [15-17]. Assembly of condensates is primarily mediated by weak, multivalent interactions between proteins with substantial disorder or conformational flexibility. These assemblies often exhibit liquid-like behavior, such as fusion, wetting, and high degrees of molecular rearrangement [17].

Recent work has shown that some cytoskeletal effectors are able to assemble into condensed phases mediated by LLPS, and these condensates are capable of driving polymerization of cytoskeletal filaments [18, 19]. For example, droplets containing Nephrin, NCK, N-WASP and Arp2/3 localize actin and actin polymerization upon addition of actin monomers [16, 20]. What role could protein droplets play in organizing cytoskeletal filaments into higher order assemblies? Here we show that VASP undergoes LLPS to form liquid-like droplets. These droplets strongly localize actin polymerization. To minimize curvature, actin filaments partition to the edges of the droplets, forming a growing ring. When the rigidity of the ring exceeds the mechanical constraints of the droplet surface tension, a linear actin bundle is formed through a series of symmetry breaking events. Guided by a continuum-scale computational model, this work describes a physical mechanism by which the unique, liquid-like properties of protein droplets can bundle cytoskeletal filaments.

RESULTS AND DISCUSSION

The tetrameric actin polymerase, VASP, forms liquid-like droplets

As a homo-tetramer, VASP has an inherent potential for multivalent interaction. Additionally, about 60% (amino acids 115-340) of VASP is predicted to be intrinsically disordered, Figure 1A, Supplemental Figure S1 [18, 21, 22]. VASP's intrinsically disordered

region has a high proline content, which may facilitate interactions with other domains of VASP or with other actin-interacting proteins [23]. These features suggest that VASP may be capable of forming extended multi-valent networks. To test this idea, we combined VASP (2-20 μM monomer concentration, ~10% labeled with Alexa-Fluor 647) with the crowding agent polyethylene glycol (PEG 8k, final concentration 3% (w/v)). Here PEG is included to mimic the crowded cytoplasm, a common practice in the LLPS field [24-27]. The final buffer, hereafter referred to as "droplet buffer", contained 50 mM Tris pH 7.4, 150 mM NaCl, 0.5 mM EDTA/EGTA, 5 mM TCEP, and 3% (w/v) PEG8K. For imaging purposes, we utilized a previously published mutant of human VASP, in which the three endogenous cysteines were replaced by two serines and an alanine, respectively. A single, exogenous cysteine was introduced at the N-terminus of the protein allowing for selective labeling using maleimide chemistry [1]. This mutant has been found to drive actin polymerization at rates indistinguishable from the wild-type protein [1]. Upon imaging with fluorescence confocal microscopy, the presence of micrometer-scale, spherical, protein-rich droplets were observed within 10 minutes of PEG addition, Figure 1B. The number and size of these droplets increased with the concentration of VASP at constant temperature, as expected for LLPS [28, 29]. Unlabeled VASP formed similar droplets to those formed from labeled protein (Figure 1C). VASP droplets fused and re-rounded, within about one second following contact, indicating their fluid-like nature, Figure 1D, Supplemental Video S1. They wetted glass coverslips that were coated with hydrophilic lipid bilayers, becoming dome-like, providing further evidence of their fluidity, Figure 1E, top. In contrast, substrates coated with polyethylene glycol were repulsive to droplets, such that the droplets remained spherical, Figure 1E, bottom. To probe the rate of molecular exchange within droplets, we measured fluorescence recovery after photobleaching (FRAP). A region of about 2 μm in diameter within VASP droplets recovered quickly and nearly completely (fractional recovery 93.9 ± 4.89%) in less than two minutes (t1/2 17.88±2.69 sec) (Figure 1F, Supplemental Video S2), indicating that molecular exchange is rapid within VASP droplets.

To evaluate the molecular determinants of phase separation by VASP, we created a series of mutants and tested their ability to form droplets (Figure 1G). We also quantified the partitioning of 1 μM of each of the mutants into droplets formed from 20 μM of full-length VASP (Figure 1H). First, because intrinsically disordered regions are in many cases sufficient to drive LLPS [30], we tested whether the intrinsically-disordered, proline-rich region of VASP alone (VASP-IDR) was capable of forming droplets. We found that VASP-IDR did not form droplets, even at a protein concentration of 100 μM and a PEG concentration of 10% (w/v), Figure 1G. Further, VASP-IDR partitioned weakly to VASP droplets, with an enrichment of 1.9-fold over background, compared to the 9.3-fold enrichment observed for self-partitioning of full-length VASP, Figure 1H. Since multivalency is critical for generating the higher order networks required for LLPS, we next tested whether monomeric VASP, which lacks the coiled-coil domain responsible for tetramerization, VASPΔtet, was capable of forming droplets. VASPΔtet was unable to form droplets, even at high protein or PEG concentrations (up to 56 μM VASP and up to 5% PEG) (Figure 1G). Additionally, VASPΔtet partitioned relatively weakly to droplets composed of full-length VASP, with a partition factor of 2.5, Figure 1H. Previous work has shown that the VASP tetramer, which relies on a coiled-coil interaction, is strong and highly stable, making VASP a native tetramer under physiological conditions [9]. Our data

suggest that tetramerization of VASP is essential for LLPS. However, to create an extended network, VASP tetramers must associate. None of the domains within VASP are known to bind to one another, suggesting that the interactions between tetramers are weak. One possibility is that the EVH1 domain, which is known to have weak binding interactions with specific proline repeat sequences [23], could interact with VASP's proline-rich IDR. However, the specific proline-motifs to which EVH1 binds are not present in the IDR, suggesting that these interactions would be very weak. Nonetheless, we constructed a mutant of VASP with the EVH1 domain deleted, VASPΔEVH1. This mutant displayed significantly impaired phase separation, as 30 μM VASPΔEVH1 was unable to form droplets at 3% PEG, but formed small droplets at 5% PEG (Figure 1I), and larger ones when the protein concentration increased to 100 μM, while maintaining 5% PEG. We also found that VASPΔEVH1 was enriched approximately 6.8-fold in VASP droplets, somewhat less than the self-partitioning of VASP, 9.3-fold (Figure 1H). These data suggest that the EVH1 domain plays a role in LLPS of VASP, perhaps by interacting with VASP's IDR, though the exact interaction remains unclear. Finally, we determined that electrostatic interactions are important to condensation of VASP, as screening these interactions with a sodium chloride concentration above 250 mM inhibited droplet formation (Figure 1I). This finding is consistent with the high density of charged residues in VASP, which may result in weak electrostatic interactions among any of its domains, helping to create a long-range network [1, 9, 31].

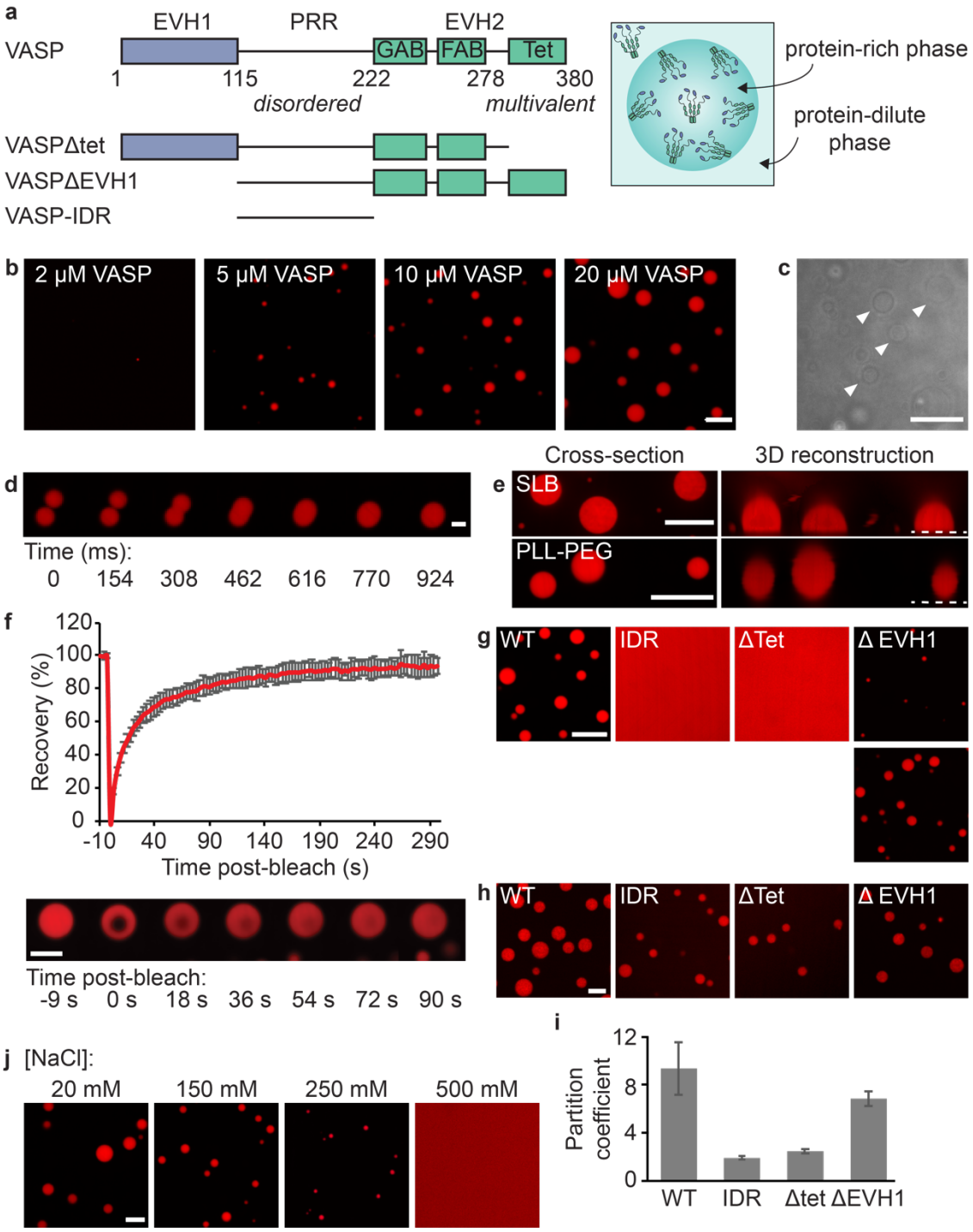

Figure 1: VASP forms liquid-like droplets in vitro. (a) *Left:* Domain organization of VASP and generated VASP mutants. *Right:* Hypothesized schematic of VASP droplet formation. (b) Droplets formed by VASP (labeled with AlexaFluor-647) at increasing protein concentrations. Scale bar 5 μm (c) Brightfield images of unlabeled 30 μM VASP droplets (arrows). Scale bar 10 μm. (d) Fusion and re-rounding of two VASP droplets. Scale bar 2 μm. (e) 20 μM VASP droplets exhibit wetting of glass coverslips passivated with supported lipid bilayers (SLB), but not PLL-PEG passivated coverslips. Scale bar 10 μm. (f) FRAP of 15 μM VASP droplets. *Top:* Recovery profile after photobleaching a 1.8 μm ROI within VASP droplets. The average recovery is 93.9 ± 4.89% (n=9 droplets; error bars are

SD). *Bottom:* Image series of fluorescence recovery of VASP droplets. Scale bar 5 μm. (g) Droplet formation of various VASP mutants. *Bottom:* Droplet formation by 100 μM VASPΔEVH1 at 5% PEG. Scale bar 10 μm. (h) Partitioning of 1 μM VASP and VASP mutants to 20 μM unlabeled VASP droplets. Scale bar 5 μm. (i) Quantification of partitioning experiments from H and I. Partitioning is defined as the ratio of protein intensity inside the droplet to outside the droplet. Bars depict averages, and error bars represent standard error across n=3 independent experiments with at least 3 images quantified per experiment. (j) Increasing salt concentration disrupts 15 μM VASP droplet formation. Scale bar 5 μm.

Polymerization of actin inside VASP droplets progressively transforms droplet shape

We next investigated the role of VASP droplets in actin polymerization and filament organization. We added G-actin monomers labeled with Atto-488 to protein droplets composed of VASP, labeled with AlexaFluor-647. We examined increasing ratios of actin to VASP including: 1:20 (1 μM actin, 20 μM VASP), 1:10 (2 μM actin, 20 μM VASP), and 1:7.5 (2 μM actin, 15 μM VASP). Under each of these conditions, actin localized strongly to VASP droplets, resulting in dramatic changes in droplet morphology, with many droplets taking on elongated shapes (Figure 2a). Notably, in the presence of the polymerization inhibitor, latrunculin A, all droplets remained spherical in shape, suggesting that actin polymerization was responsible for the changes in droplet morphology, Figure 2b. In the absence of latrunculin A, about 10-15 minutes after addition of actin, we observed several distinct droplet morphologies, including: (i) a homogeneous distribution of actin within spherical droplets, (ii) peripheral accumulation of actin at the inner surfaces of spherical droplets, (iii) deformation of actin-filled droplets into ellipsoid shapes, and (iv) rod-like, actin-filled droplets, Figure 2c. The distribution of these morphologies changed as the actin to VASP ratio increased, Figure 2d. Specifically, for an actin to VASP ratio of 1:20, most VASP droplets were spherical with homogeneous or peripheral actin distributions. As this ratio increased to 1:10, elliptical and rod-like morphologies emerged, with elliptical droplets making up the majority. Finally, for a ratio of 1:7.5, most droplets had elongated shapes, with more than half taking on rod-like morphologies. Time-lapse imaging of VASP droplets after addition of actin revealed that actin rearranged within droplets from an initially homogeneous distribution to a peripheral distribution (Figure 2e and Supplemental Video S3) and that droplets with a peripheral distribution of actin frequently transformed into ellipsoid and rod-like morphologies, Figure 2f and Supplemental Video S4. Collectively these data demonstrate that actin polymerization within VASP droplets drives peripheral accumulation of actin, followed by a progressive increase in droplet aspect ratio, leading to actin-filled droplets with elliptical and rod-like shapes. To better understand the impact of actin polymerization on droplet morphology, we sought to examine each of these transitions in greater detail, beginning with the peripheral accumulation of actin at the inner surfaces of VASP droplets.

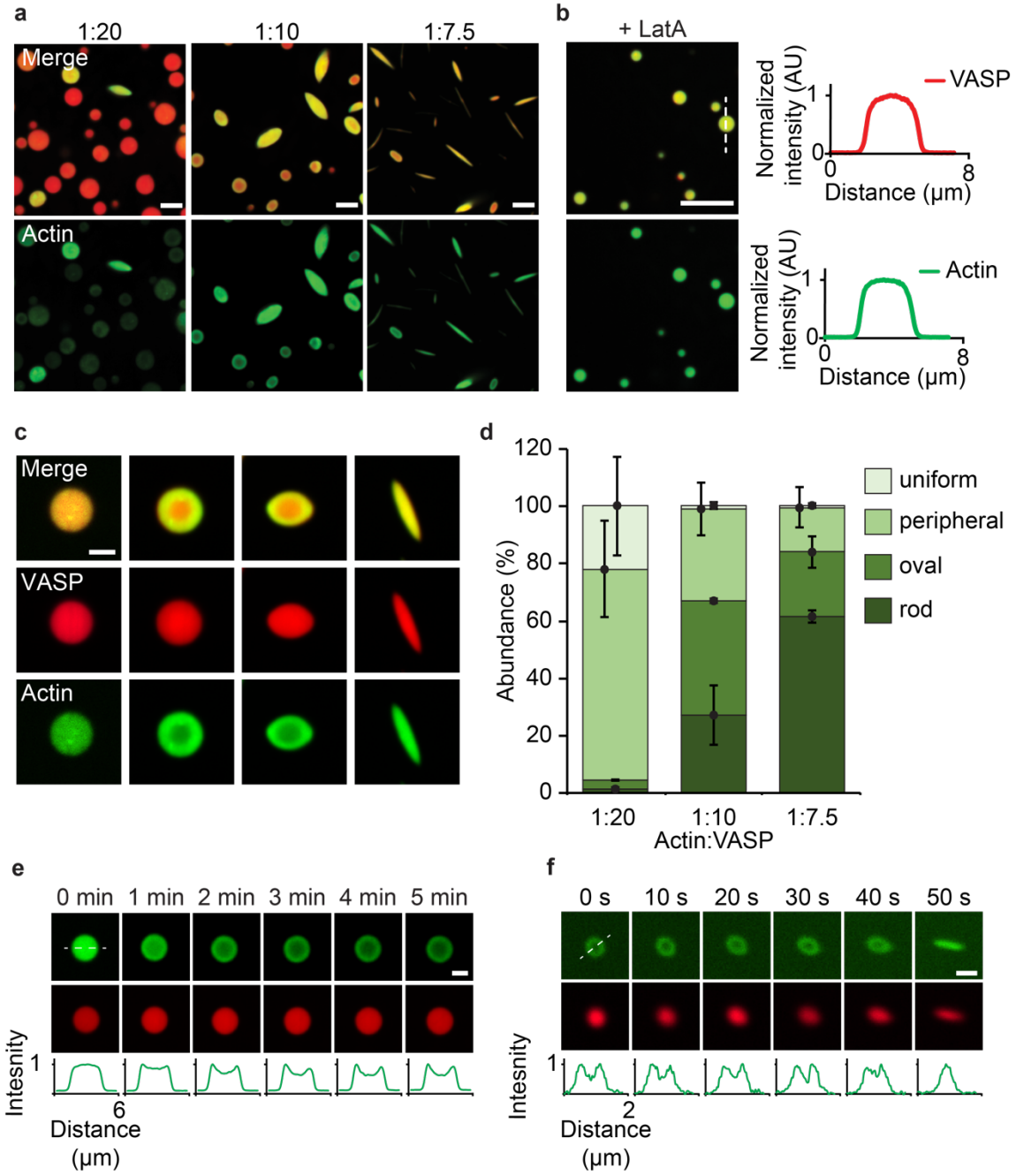

Figure 2: Actin polymerization within VASP droplets drive droplet deformation through discrete intermediates. (a) Increasing actin to VASP ratio results in increasingly elongated structures. Scale bar 5 μm. (b) Pretreatment of VASP droplets with 5 μM LatrunculinA inhibits actin polymerization and results in the uniform partitioning of actin to VASP droplets. Scale bar 10 μm. Line profile of actin and VASP intensities inside the droplet. Intensity is normalized to the max intensity of each channel. (c) Representative images of the different organizations of actin in VASP droplets. From left to right: uniform, peripheral, oval and rod. Scale bar 2 μm. (d) Quantification of the percent abundance of shapes observed across increasing actin to VASP ratios tested in A. Error bars represent standard deviation across 3 independent experiments. In total, for 1:20 ratio n = 1523 droplets, for 1:10 ratio, n = 934 droplets, and for 1:7.5 n = 624 droplets were counted. (e) Time-lapse of peripheral actin accumulation in VASP droplets. Scale bar 2 μm. Line profile of actin intensity over time. Actin intensity

is normalized to the max intensity in each frame. (f) Time-lapse of deformation of droplets with peripheral actin distribution to form rod-like droplets. Scale bar 1 μm. Line profile of actin intensity over time. Actin intensity is normalized to the max intensity in each frame.

Actin polymerizes to form shells and rings inside VASP droplets

We next examined the partitioning of actin to the inner surfaces of VASP droplets. Shortly after the addition of actin, we observed polymerization of individual actin filaments within VASP droplets, Figure 3a. As filaments grew within the droplets, they began to partition to the inner surfaces of the droplet. This peripheral distribution of actin appeared similar whether actin was labeled by inclusion of fluorescent-tagged actin monomers (Atto-488), or by phalloidin, which selectively stains polymerized actin filaments, Figure 3b. The peripheral accumulation of actin resulted in assembly of three-dimensional actin shells and two-dimensional actin rings within the droplets, Figure 3c. Both structures appeared ring-like in individual confocal images but were distinguishable in three-dimensional reconstructions. In some cases, actin rings appeared to deform VASP droplets into two-dimensional discs. This observation suggests that as filaments accumulate at the droplet periphery and form a ring, their collective rigidity is sufficient to deform the droplet, Figure 3c, bottom. Among structures with peripheral actin, the distribution of shells, rings, and discs shifted from predominately shells to predominately discs and rings, as the actin to VASP ratio increased. These data suggest that shells matured to form rings and discs as actin was added, Figure 3d.

Interestingly, the thickness of actin rings within spherical droplets increased with increasing droplet diameter, Figure 3e. Further, for a given droplet diameter, droplets that had deformed into either discs (Figure 3e, Supplemental Figure S2) or ellipsoids (Figure 3f, aspect ratio above 1.1) contained thicker rings in comparison to spherical droplets. This trend implies that as the thickness of actin rings increased, the droplets began to deform. Specifically, as actin rings became thicker and more rigid, the energy required to confine them within droplets must eventually exceed the surface energy of the droplet, resulting in deformation. Notably, surface energy, the product of surface area and surface tension, increases with increasing droplet diameter, helping to explain why larger droplets can withstand thicker rings before deforming. To better understand these mechanisms, we next constructed a simple mechanical model.

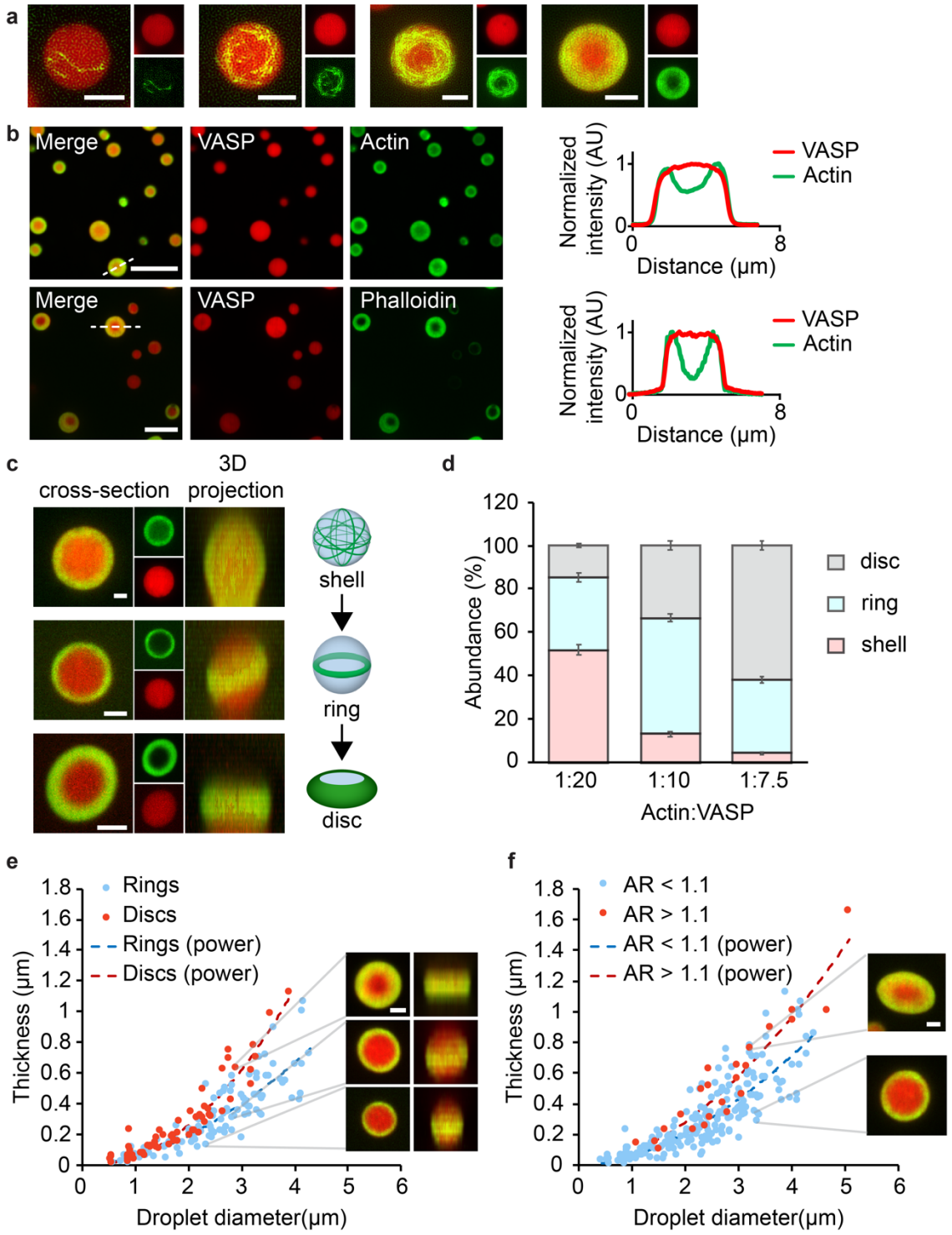

Figure 3: Peripheral accumulation of actin drives assembly of actin shells, rings, and discs. (a) Representative images of VASP droplets containing an increasing amount of filamentous actin, as stained with phalloidin. Scale bar 2 µm. (b) *Top:* Addition of 1 µM actin to 20 µM VASP droplets results in the formation of a majority of peripheral actin within the droplet. Line profile of actin and VASP intensities inside the droplet. Scale bar 10 µm. *Bottom:* Phalloidin staining of peripheral actin within VASP droplets. Line profile of phalloidin-actin and VASP intensities inside the droplet. Scale bar 5 µm.

Intensity is normalized to the max intensity of each channel. (c) Representative images of VASP droplets containing peripheral actin distribution. Peripheral actin, as observed with phalloidin staining, distribution can be further classified as shells, rings, or discs, as observed by 3D reconstructions. Scale bar 2 μm. (d) Quantification of the abundance of shells, rings, and discs as a function of actin to VASP ratio. Error bars represent standard deviation, where n = 302 total droplets counted across at least 6 images per condition. (e) Quantification of ring thickness as a function of droplet diameter, for disc and ring distributions of actin. Trendline represents the best fit to a power law of the form $y = ax^b$. For rings, a = 0.0558 and b = 1.7922, R^2 = 0.7499 (n=109 droplets). For discs, a = 0.0594, b = 2.1412, R^2 = 0.9047 (n=62 droplets). (f) Quantification of ring thickness as a function of droplet diameter, sorted by droplet aspect ratio. Trendline represents the best fit to a power law of the form $y = ax^b$. For droplets with AR < 1.1, a = 0.0624 and b = 1.7580, R^2 = 0.7185 (n=206 droplets). For droplets with AR > 1.1, a = 0.08326, b = 1.7675, R^2 = 0.8949 (n=23 droplets).

A continuum-scale computational model explains the mechanics of droplet deformation by actin

Filamentous actin has been previously observed to accumulate and form rings at the inner surfaces of spherical containers such as membrane vesicles and aqueous/oil emulsions [32, 33]. In these cases, partitioning of actin to the container surface was observed whenever the diameter of the container was less than the persistence length of actin filaments, 10-20 μm. This criterion is met by the VASP droplets in Figures 2 and 3, which ranged in diameter from 1-7 μm, Supplemental Figure S3.

In the case of a growing filament within a spherical container, the relative stiffness of the filament determines whether the filament deforms the interface or bends to fit within the container [34]. For filaments that remain within the container, the lowest energy state for the bent filament is reached when the filament partitions to the edge of the droplet, where it experiences the least curvature. This partitioning should lead to a shell of curved filaments at the inner surface of the droplet, as observed in Figure 3. The transition from a shell to a ring has been previously observed in the presence of either macromolecular depletants or actin bundling proteins [33]. Similarly, our observation of actin rings can be explained by both the crowded nature of the droplet interior and the ability of VASP to bundle actin filaments.

The total energy of the ring, including contributions from thermal fluctuations and filament bending, is given by Equation 1.

$$\boldsymbol{E_{bend}} = \frac{\boldsymbol{k_b}}{\boldsymbol{2}}\left(\frac{\boldsymbol{L}}{\boldsymbol{R^2}} + \frac{\boldsymbol{L}}{\boldsymbol{R^4}}\sum_{\boldsymbol{m}}(\boldsymbol{2} + \boldsymbol{m^4})\boldsymbol{u_m^2}\right) \quad (1)$$

Here, k_b is the ring bending rigidity, which we assume is directly proportional to the number of filaments in each ring. $1/R$ is the filament curvature where R is the droplet radius, and L is the filament length. The second term in Equation 1 represents the contributions from thermal fluctuations of the droplet-filament interface, where m is the Fourier mode and u_m is the Fourier amplitude and is given by equipartition theorem as, $u_m \approx \frac{R^2}{\sqrt{LL_p}}$. L_p is the persistence length of the filaments. We assume that the thickness of the ring in a spherical droplet is proportional to the Fourier amplitude u_m of the bundle. Hence, the droplets with larger ring thicknesses cannot remain spherical and will deform. See Supplementary materials for the full derivation [32, 35] . This analysis, which builds on the work of Limozin et al [32], predicts that the ring thickness scales quadratically with the

droplet radius. Additionally, when the ring length L matches the droplet circumference, ring thickness is predicted to scale as $D^{1.5}$. Consistent with the model predictions, studies have shown that the exponent ranges between 1.5 and 2. [32, 35 36]

As noted above, actin polymerization was confined to VASP droplets and did not occur in the surrounding solution, Figure 2. This confinement implies that the wetting energy of actin in the VASP-rich phase, γ_{AVR}, is significantly lower than the wetting energy of actin in the VASP-dilute phase, γ_{AVD}. There is an additional energy component to consider, the interaction of VASP-rich droplet with the surroundings, γ_I, which determines the shape of the droplet interface, effectively giving a surface energy for a droplet of surface area A_I, as $E_I = \gamma_I A_I$. As long as the ring bending energy, E_{bend}, is less than E_I, the droplet will retain its spherical shape. This reasoning suggests that when E_{bend} exceeds E_I, the shape of the droplet must change to accommodate the change in the filament curvature.

We modeled the interaction energies between the actin filaments and VASP droplets using a numerical energy minimization scheme written in Python (see Supplemental Figure S4 for details). For simplicity, we assume that the droplet is a 2D circle and the filament ring is represented by a curve with finite thickness, Figure 4a-b. Additionally, we assume that the ring thickness is uniform along the entire length of the ring thereby approximating the ring as a 1D curve. We establish the ring confinement within the droplet by carefully tuning the values of γ_{AVR} and γ_{AVD}, Figure 4d, and Supplemental Figure S5). As we increased the ring thickness (Figure 4e bottom), for a fixed droplet radius and γ_I, the shape of the droplet changed from a circle to an ellipse, Figure 4f. This behavior held for a range of droplet diameters, demonstrating its generality, Figure 4g. To determine whether these relationships held for different values of γ_I, we varied γ_I for droplet diameters ranging from 0.5 – 4 μm. For each combination of droplet diameter and γ_I, we plotted the aspect ratio of the resulting droplet as a function of increasing ring thickness, Figure 4g (additional γ_I values in Supplemental Figure S6). Additionally, to identify the threshold of droplet deformation, we plotted the ring thickness above which the circular droplet began to deform as a function of droplet diameter for a range of γ_I(aspect ratio greater than 1.1). Here we found that the threshold ring thickness increased non-linearly with increasing droplet diameter in good agreement with the experimental data in Figure 3e (rings). In particular, as droplet radius increases, surface energy increases, such that thicker rings are required to deform droplets.

Once droplets take on elliptical shapes, how do they transition into linear, rod-like structures? This 2D to 1D transition can be understood as a further minimization of the bending energy of the filaments at the expense of surface energy. A mechanical argument for this idea is provided in the Supplemental Material. Briefly, for a droplet of circular cross-section, the radius of curvature is uniform everywhere and therefore, the bending energy is spatially homogeneous, as in the case of an actin ring. However, as a droplet begins to elongate, the elliptical cross-section has regions of high curvature and regions of low curvature. For an elliptical cross-section with major axis 2a and minor axis 2b, the maximum curvature, along the major axis, is a/b^2 and the minimum curvature is b/a^2. This curvature heterogeneity is rather pronounced as the droplet aspect ratio increases, Supplemental Figure S7. Rather than bend over the highly curved interface along the major axis, at a certain aspect ratio, it becomes energetically more favorable for the ring to straighten into a rod. Thus, the spatial variations of actin dynamics and actin-VASP

interactions are now confined to one-dimension. In the next section we examine the resulting higher aspect ratio structures and compare them with the predictions of these simple models.

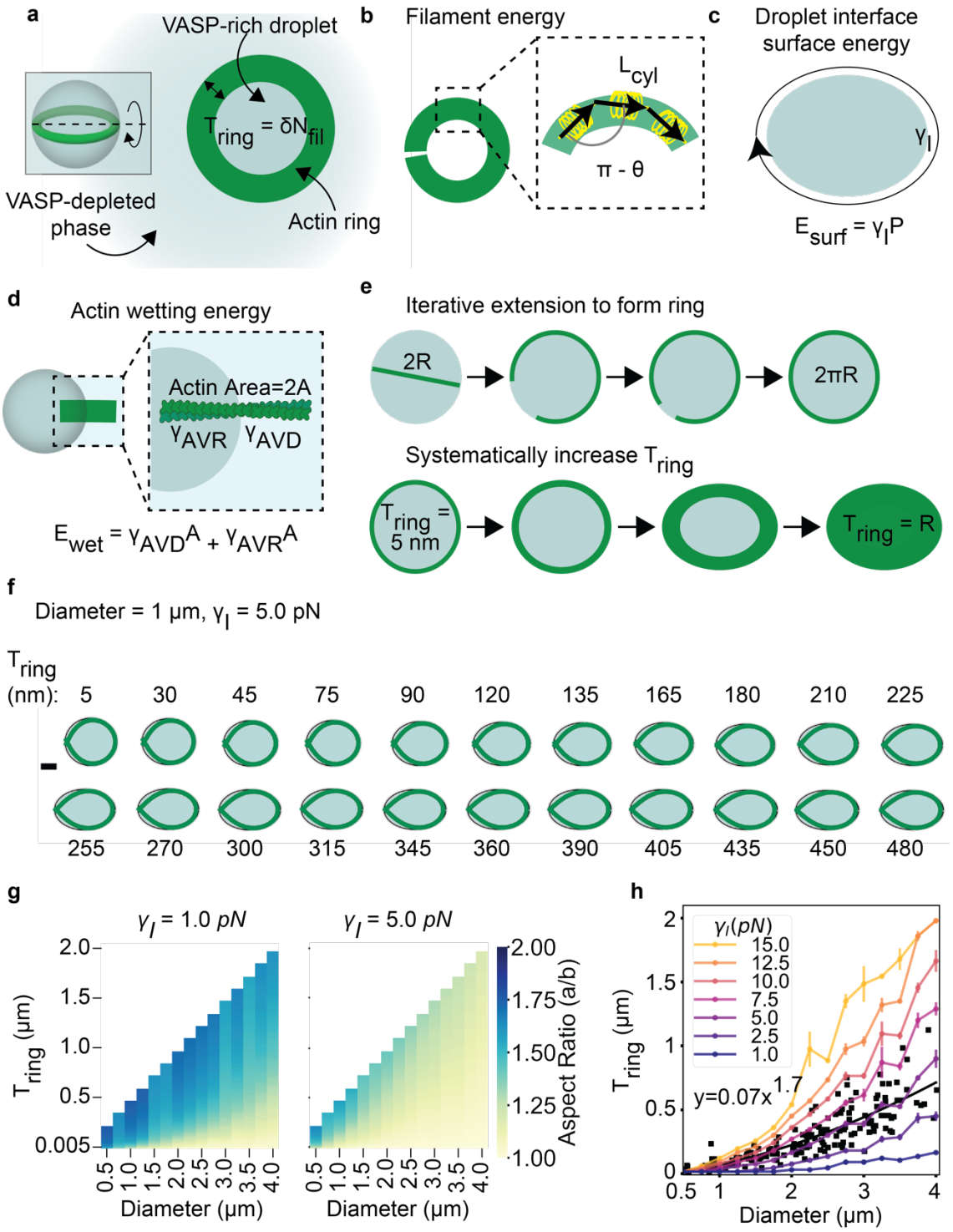

Figure 4. An elastic model predicts shape changes by balancing filament bending energy and droplet surface energy. (a) Cartoon shows a VASP-rich droplet phase embedded in a VASP-depleted background. Droplet also contains an actin ring (green). (b) Illustration of filament energy. Actin ring is represented as a linear chain discretized into segments of length L_{cyl} that can bend around hinge points. The stretching constant (k_{str}) and the bending constant (k_{bend}) are assumed to scale linearly with the number of filaments in the ring. (c) Illustration of VASP surface energy. The perimeter (P) of the VASP-rich droplet phase can change subject to surface energy parameter (γ_I). (d) Illustration of actin wetting energy terms. Panel shows an actin ring of area 2A wetted by the VASP-dilute phase (AVD) and VASP-rich phase (AVR). Their interaction strengths are represented respectively by γ_{AVD} and γ_{AVR} respectively. The actin ring interacts exclusively with the VASP-rich phase as long as $\gamma_{AVR} << \gamma_{AVD}$ as explained in Supplemental Methods. (e) Cartoon shows the 2d plane of ring formation from panel a. Proposed 2D model accounts for changes due to actin deposition onto a preexisting ring. *Top:* Cartoon shows protocol to obtain an actin ring embedded in a 2d droplet. Droplets are initialized with a single actin filament of length 2R. The length of filament is iteratively increased in steps of 100 nm and the resulting system is energy minimized subject to energies explained in panels b-d to eventually obtain an actin ring embedded in a VASP droplet. *Bottom:* Cartoon shows a protocol to study shape changes at various ring thickness values. Using the ring obtained from the protocol in panel c1 as the initial condition, we iteratively increase the ring thickness by 15 nm to generate the shape of the droplet-actin ring system at minimum energy configuration. (f) Subpanels show the predicted shape of the droplet of initial radius 1 μm, and γ_I=5.0pN when the actin ring thickness is increased from 5nm to 0.48μm. Scale bar = 0.25μm. The interface between the VASP-rich droplet and the VASP-depleted background is shown in black. VASP rich droplets are colored in blue while the actin ring is shown in green. The thickness of the actin ring does not correspond to the T ring values used. (g) Heatmap shows the predicted aspect ratios of droplets of various initial diameters at various actin ring thicknesses and droplet diameter. (h) Plot shows the predicted mean and standard deviation ring thickness above which we observe the circle-ellipse shape transition (Shape is deemed elliptical when aspect ratio>1.1) at any given droplet diameter and droplet interfacial surface tension, γ_I. Experimentally observed aspect ratios are overlaid as a scatter plot with black squares. Black solid line represents the trendline from a power law fit to the experimental data.

At higher actin to VASP ratios droplets become elongated by actin polymerization

The computational model predicts that the aspect ratio of VASP droplets should increase with increasing stiffness of the actin rings that they encapsulate. The validity of this prediction is directly demonstrated by the data in Figure 3f, showing that droplets with higher aspect ratios contain thicker, and therefore stiffer, actin rings. However, this analysis was confined to structures of relatively low aspect ratio (< 2.5) because increasing aspect ratio leads to narrowing of the droplet minor axis such that actin rings can no longer be resolved, Figure 2a (1:7.5). Nonetheless, the model in Figure 4 predicts that the aspect ratio of these structures should continue to increase with increasing actin content. To examine this idea, we plotted the distribution of droplet aspect ratios for each of the actin to VASP ratios examined in Figure 2a, 1:20, 1:10, and 1:7.5. As expected, we found that the median aspect ratio increased significantly with increasing actin to VASP ratio, Figure 5a.

Examining the images in Figure 2a, it is apparent that droplets with higher actin content generally had higher aspect ratios. Variations in actin content likely arise from competition among droplets for actin, where droplets that sequester enough actin to drive polymerization attract more actin monomers at the expense of droplets that have yet to reach polymerization threshold. Notably, in the presence of latrunculin A, which prevents actin polymerization, the distribution of actin among VASP droplets was highly uniform,

suggesting that polymerization of actin gave rise to the differences in actin intensity between droplets, Figure 2. The spontaneous variation in actin intensity among the droplets presents an opportunity to examine the impact of actin concentration on droplet aspect ratio in situ for each actin to VASP ratio. To study this effect, we plotted droplet aspect ratio as a function of actin intensity, Figure 5b, Supplemental Figure S8 Here, as expected, droplet aspect ratio increased with actin intensity. Interestingly, data from different actin to VASP ratios overlay on a single trend, each populating increasing, yet overlapping ranges of actin intensity. This result suggests that actin concentration within the droplet is the major variable controlling aspect ratio, regardless of the bulk actin and VASP concentrations. The sharp rise in aspect ratio with increasing actin intensity suggests that there may be a critical actin concentration threshold, beyond which aspect ratio increases rapidly.

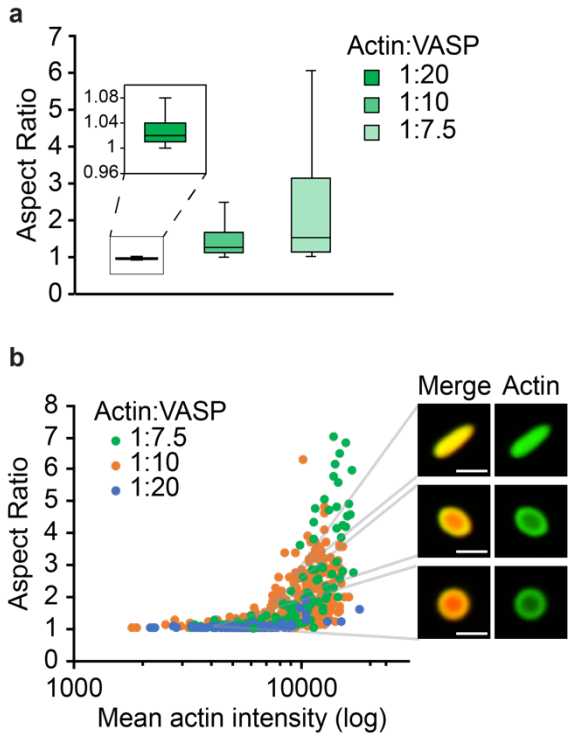

Figure 5: Increasing the actin concentration within the droplet drives droplet deformation into elongated structures**.** (A) Distribution of droplet aspect ratios observed across increasing actin to VASP ratios. Box represents interquartile range (IQR), with median as a bisecting line. Whiskers represent range of data points that are within 1.5*IQR larger than Q3 or 1.5*IQR smaller than Q1. At least 400 droplets were counted across n = 3 independent experiments per condition. (B) Quantification of the dependence of droplet aspect ratio on actin intensity within the droplet (n = 626 droplets analyzed across at least 3 images per condition). Scale bar 2 μm.

VASP droplets bundle actin filaments and exhibit liquid-like behavior

Actin organizes into long bundles of very high aspect ratio in cellular structures such as filopodia [37] and stress fibers [38]. Therefore, we next investigated the impact of higher actin content on droplet aspect ratio. Specifically, we formed droplets from a solution of 10 μM VASP and added 2 μM of actin to achieve a 1:5 ratio of actin to VASP. Under these

conditions we observed rapid deformation of initially spherical droplets into thin, linear structures with aspect ratios that frequently exceeded 20:1, Figure 6a, b. Actin colocalized with VASP throughout the growth of these structures, suggesting that the droplet deformed and grew continuously with the growing actin filaments, Figure 6c. The rate at which the structures increased in length was highly linear, and structures grew simultaneously from both ends at equal rates, Figure 6a-c, Supplemental Video S5. This observation suggests that barbed ends pointed away from the droplet along both axes of the elongated structures. The constant growth rate of the structures suggests that the actin filaments within them were oriented in a co-linear, bundle-like fashion. The average growth rate in the presence of ATP was 21 +/- 2 nm/s, about 8 monomers per second, Figure 6d. This rate is several fold slower than the rates of VASP-catalyzed single filament elongation found in the literature [1, 39]. The slower growth rate could arise from several factors including the viscosity of the droplet environment, which could slow the diffusion of new actin monomers to filament tips, and the possibility that not all filaments grow simultaneously, perhaps owing to competition for a limited supply of actin. Interestingly, when growing actin bundles encountered one another, they “zippered” together within seconds, presumably to minimize the surface energy of the VASP droplets in which they were confined, Figure 7a, Supplemental Video S6. This behavior suggests that the liquid-like nature of VASP droplets persists, despite severe deformation by growing actin bundles. Additionally, the zippering of bundles upon contact provides an additional mechanism of filament alignment, as it is capable of merging individual bundles to create thicker structures.

To further probe the physical properties of actin bundles encased within VASP droplets, we performed FRAP experiments. When the tips of growing bundles were bleached, the VASP signal recovered within 3 minutes, suggesting that the VASP phase remained liquid-like. In contrast, the actin signal in the bleached region did not recover significantly, as expected for stably polymerized filaments, Figure 7b,c (Supplemental Video S7). However, the bundles continued to grow after bleaching and the regions of new growth were clearly visible in the actin channel, suggesting that they consisted of actin monomers that originated from outside the bleached region, likely from the surrounding solution. A significant increase in actin signal was not observed anywhere else along the bundle, suggesting that addition of new actin monomers was confined to the tips of bundles, similar to the growth of actin filaments inside filopodia[40 41]. Finally, we performed FRAP on spherical droplets, just as they were beginning to transform into bundles, Figure 7d and Supplemental Video S8. Under these conditions, as the droplet deformed, the total actin intensity increased dramatically during growth of the bundle, greatly exceeding the initial actin intensity of the droplet before it was bleached, Figure 7e. Meanwhile, the intensity in the VASP channel also exceeded its initial value, albeit more modestly. These results demonstrate the ability of the VASP droplet to template filament alignment. In particular, once growing actin filaments become aligned within a VASP droplet, the parallel orientation of filaments propagates during the growth of the bundle as new material from outside the initial droplet is incorporated. In this way, even a small droplet of VASP can setup a parallel orientation of actin filaments that will persist over much longer length scales.

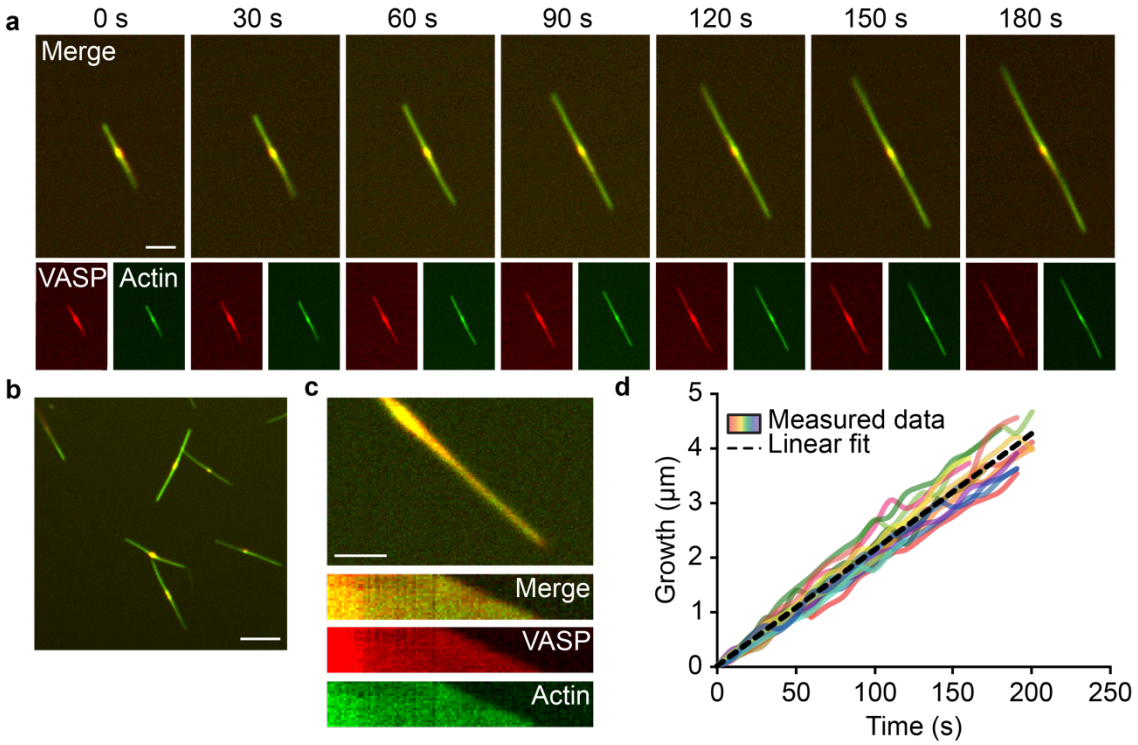

Figure 6: Droplets formed at high actin to VASP ratios bundle actin filaments. (a) Addition of 2 µM actin added to 10 µM VASP droplets results in linear droplets that elongate over time. Scale bar 5 µm. (b) Representative image of linear droplets generated after adding actin to VASP droplets. Scale bar 5 µm. (c) Representative image (top) and associated kymograph (bottom) of a linear droplet elongating over time. Scale bar 1 µm. (d) Quantification of the elongation rates of linear droplets (n= 18 droplets). Trendline represents the linear fit of the average across all droplets. Linear fit y = 0.0213x R^2 = 0.9994.

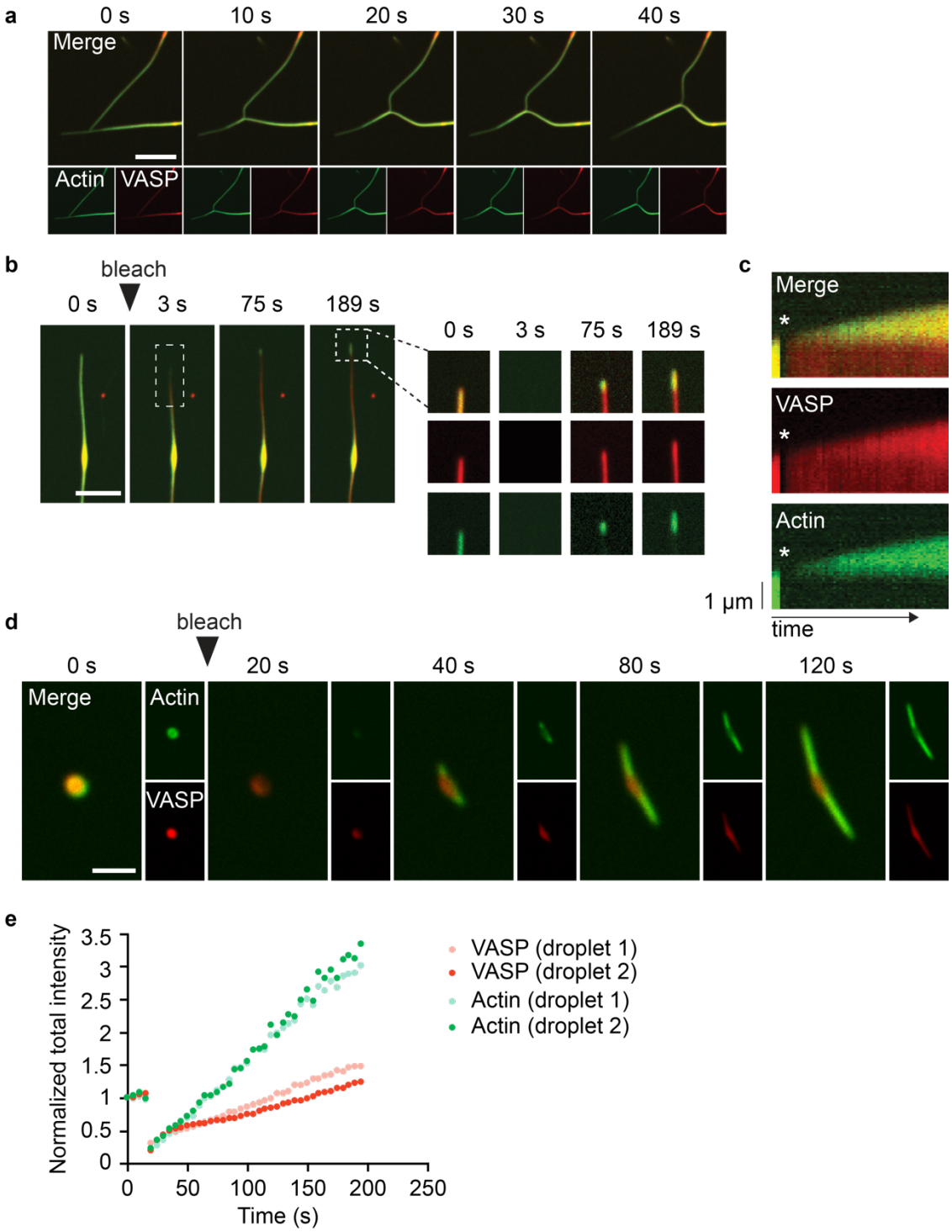

Figure 7: Droplet bundles display dynamic properties. (a) Droplet bundles that come in contact zipper together to form a thicker bundle. Scale bar 5 µm. (b) Photobleaching of the ends of the elongating droplets results in recovery at the tips of the bundle. Dotted white box indicates bleach region. Scale bar 2 µm. (c) Kymograph of the recovery profile of the droplet bleached in B. Asterisk denotes the bleach frame. (d) Photobleaching of a round droplet that subsequently undergoes transformation into a rod. Scale bar 2 µm. (e) Quantification of the total actin and VASP intensity in the structure over time, as seen in d. Total actin intensity is the result of summing the pixel intensities across the droplet and normalizing to the pre-bleach total intensity.

DISCUSSION

Here we show that the actin polymerase, VASP, assembles into liquid-like droplets that polymerize and bundle actin. Polymerization of actin inside these droplets drives a series of morphological transformations from spherical droplets with shell and ring-like actin distributions to deformation of the surrounding droplets into discs, ellipsoids, rods, and finally linear bundles of parallel filaments. These transformations can be understood by minimizing the energy of the filament-droplet composite, as illustrated by a continuum-scale computational model.

Previous work has shown that non-specific interactions between actin and the surfaces of protein droplets can concentrate actin, driving its polymerization outside of droplets [42], and that incorporation of short, pre-polymerized filaments can promote filament alignment, leading to nematic crystals that promote tactoid-like droplet morphologies [43]. In contrast, our work illustrates the potential of droplets to couple actin polymerization to alignment of filaments, ultimately leading to droplet-encapsulated filament bundles. Earlier studies illustrated that droplets of the tau protein can nucleate microtubule polymerization, ultimately leading to filament alignment [44]. However, microtubules, which have persistence lengths on the millimeter scale [45], are far too rigid to organize within droplets by the mechanisms that we have illustrated for actin filaments, suggesting that a simpler mechanism, driven solely by the minimization of droplet surface energy, may be responsible.

In contrast, our primary finding is that liquid-like protein droplets can mediate the bundling of highly flexible actin filaments through a mechanism in which the rigidity of a growing filament bundle competes against the finite surface energy of the droplet. In particular, our data illustrate how a droplet can locally concentrate actin and organize it into a ring-like bundle. Then, as the thickness of the ring increases, its bending rigidity eventually overcomes the surface tension of the droplet, resulting in deformation of the droplet and transformation of the bundle into a linear structure with a constant polymerization rate. The observation that growing bundles zipper together upon contact illustrates the liquid-like nature of the surrounding VASP droplet, and provides an additional mechanism that promotes bundling.

VASP associates with aligned actin filaments in multiple cellular structures including filopodia and focal adhesions [46, 47]. Interestingly, multiple proteins involved in assembly of focal adhesions have recently been found to undergo liquid-liquid phase separation [48-50] . However, the role of this network in aligning actin filaments is presently unknown. Our work builds on this understanding by demonstrating a new physical mechanism by which VASP, and potentially other actin interacting proteins, can harness phase separation to align filaments.

MATERIALS & METHODS

Reagents. Tris base, NaCl, EDTA, EGTA, TCEP, poly-L-lysine, Atto 594 maleimide, catalase, glucose oxidase were purchased from Sigma-Aldrich. Alexa Fluor 647 C2 maleimide was purchased from Thermo Fisher Scientific. Phalloidin-iFluor488 was purchased from Abcam. Amine-reactive PEG (mPEG–succinimidyl valerate MW 5000) was purchased from Laysan Bio. Rabbit muscle actin was purchased from Cytoskeleton.

Cloning and protein purification. A pET vector encoding the "cysteine light" variant of human VASP (pET-6xHis-TEV-KCK-VASP(CCC-SSA)) was a generous gift from Scott Hansen. All VASP mutants were generated using this plasmid as a template. pET-6xHis-TEV-KCK-VASPΔtet encoding monomeric VASP was generated by using site directed mutagenesis to introduce a stop codon after residue 339 to generate a truncated version of VASP lacking residues 340-380 corresponding to the tetramerization domain. The forward primer: "GCTCCAGTTAGTACTCGGACCTACAGAGGG" and reverse primer "GTCCGAGTACTAACTGGAGCTGGGCGTG. pET-6xHis-TEV-KCK-VASPΔEVH1 encoding VASPΔEVH1 was generated by PCR mediated deletion of the EVH1 domain (residues 1-113). The 750 base pairs corresponding to the EVH1 domain were deleted using the forward primer: "GACTAAGCGGCCGCGAAGGAGGTGGGCCCC" and reverse primer: "GACTAAGCGGCCGCCTTTACATTTGGATCCCTGGAAGTACAG" that both encoded NotI cut sites. After PCR amplification and purification, the amplicon was digested with NotI and recircularized to generate the resulting product. pGEX-6P1-KCK-IDR encoding the intrinsically disordered, proline-rich region of VASP was generated by restriction cloning. Amplification of the IDR (residues 115-222) was achieved using the forward primer: "CAACGAGGATCCAAATGTAAAGGAGGTGGGCCCCCTCCAC" and reverse primer: "TAATATCTCGAGTAATTACCCAGCTCCCCCACCACCAGGG". The amplicon was then inserted into the pGEX-6P1 vector at the BamHI and XhoI restriction sites.

The pET-His-KCK-VASP(CCC-SSA) plasmid was transformed into *E. coli* BL21(DE3) competent cells (NEB Cat#C2527). Cells were grown at 30ºC to an OD of 0.8. Protein expression was performed as described previously with some alteration [1]. Expression of VASP was induced with 0.5mM IPTG, and cells were shaken at 200 rpm at 12ºC for 24 hours. The rest of the protocol was carried out at 4ºC. Cells were pelleted from 2L cultures by centrifugation at 4785 x g (5000 rpm in Beckman JLA-8.100) for 20 min. Cells were resuspended in 100ml lysis buffer (50mM sodium phosphate pH 8.0, 300mM NaCl, 5% Glycerol, 0.5mM TCEP, 10mM imidazole, 1mM PMSF) plus EDTA free protease inhibitor tablets (1 tablet/50ml, Roche cat#05056489001), 0.5% Triton-X100, followed by homogenization with a dounce homogenizer and sonication (4x2000J). The lysate was clarified by ultracentrifugation at 125,171 x g (40K rpm in Beckman Ti45) for 30 min. The clarified lysate was then applied to a 10ml bed volume Ni-NTA agarose (Qiagen Cat#30230) column, washed with 10xCV of lysis buffer plus EDTA free protease inhibitor tablets (1 tablet/50ml), 20mM imidazole, 0.2% Triton X-100, followed by washing with 5xCV of lysis buffer plus 20mM imidazole. The protein was eluted with elution buffer (50mM Tris, pH 8.0, 300mM NaCl, 5% Glycerol, 250mM imidazole, 0.5mM TECP, EDTA free protease inhibitor tablets (1 tablet/50ml)). The His-tag was cleaved by dialyzing the

protein overnight with 1mg (10,000 units) of TEV protease in 1L of cleavage buffer (50mM Tris pH 8.0, 200mM NaCl, 5% Glycerol, 0.5mM EDTA, 1mM DTT). The His-tag, uncut protein, and TEV protease were removed by a second Ni-NTA column. The protein was further purified by size exclusion chromatography with Superose 6 resin. The resulting purified KCK-VASP was eluted in storage buffer (25mM HEPES pH 7.5, 200mM NaCl, 5% Glycerol, 1mM EDTA, 5mM DTT). Single-use aliquots were flash-frozen using liquid nitrogen and stored at -80ºC until the day of an experiment. The his-tagged VASP mutants were purified using the same protocol as above as indicated or with the following modifications: His-KCK-VASPΔTet: no modifications. His-KCK-VASP-CRY2: the pH of all the buffers was changed to 8.5.

The pGEX-GST-KCK-VASP-PRR plasmid was transformed into *E. coli* BL21 competent cells (NEB Cat#C2530). Cells were grown at 30ºC to an OD of 0.8. Protein expression was induced with 0.9mM IPTG, and cells were shaken at 200 rpm at 30ºC for 6-8 hours. The rest of the protocol was carried out at 4ºC. The cells were pelleted from 2L cultures by centrifugation at 4785 x g (5000 rpm in Beckman JLA-8.100) for 20 min. Cells were resuspended in 100ml lysis buffer (20mM Tris pH 8.0, 350mM NaCl, 10mM KCl, 5% Glycerol, 5mM EDTA, 5mM DTT, 1mM PMSF) plus EDTA free protease inhibitor tablets (1 tablet/50ml, Roche cat#05056489001), 1.0% Triton-X100, followed by homogenization with a dounce homogenizer and sonication (4x2000J). The lysate was clarified by ultracentrifugation at 125,171 x g (40K rpm in Beckman Ti45) for 30 min. The clarified lysate was then applied to a 10ml bed volume Glutathione Sepharose 4B (Cytiva Cat#17075605) column, washed with 10xCV of lysis buffer plus 0.2% Triton X-100, EDTA free protease inhibitor tablets (1 tablet/50ml), followed by washing with 5xCV of lysis buffer. The protein was eluted with lysis buffer plus 15mM reduced glutathione, EDTA free protease inhibitor tablets (1 tablet/50ml). The GST-tag was cleaved by exchanging the protein into 20mM Tris pH 8.0, 350mM NaCl, 10mM KCl, 5% Glycerol, 5mM EDTA, 1mM DTT using a Zeba desalting column (Thermo Scientific cat#89891), adding PreScission protease (Thermo Scientific: cat 88946, 2unit/0.2mg fusion protein), and rocking gently overnight at 4ºC. The GST-tag, uncut protein, and PreScission protease were removed by a second Glutathione Sepharose 4B column. The protein was further purified by size exclusion chromatography with Superose 6 resin. The resulting purified KCK-VASP was eluted in storage buffer (20mM Tris, pH 8.0, 200mM NaCl, 5% Glycerol, 1mM EDTA, and 5mM DTT). Single-use aliquots were flash-frozen using liquid nitrogen and stored at -80ºC until the day of an experiment.

GST-KCK-VASPΔEVH1 was purified using the same protocol as above, but with the following buffer modifications: Lysis Buffer=20mM Tris pH 8.5, 350mM NaCl, 5% Glycerol, 5mM EDTA, 5mM DTT, 1mM PMSF; Storage Buffer=25mM HEPES, pH 7.5, 200mM NaCl, 5% Glycerol, 1mM EDTA, and 5mM DTT.

Protein labeling. VASP and associated VASP mutants were selectively labeled at the single N-terminal cysteine residue using maleimide conjugated dyes. Protein was incubated with a 3-fold molar excess of dye for 2 hours at room temperature to achieve a 10-20% labeling ratio. The protein was separated from the free dye by applying the labeling reaction to a Princeton CentriSpin size exclusion column (Princeton

Separations). Labeled VASP VASPΔtet, and VASPΔEVH1 were stored in 50 mM Tris pH 7.8, 300 mM NaCl, 0.5 mM EDTA 0.5 mM EGTA, 5 mM TCEP, and VASP-IDR was stored in 25 mM HEPES pH 7.1 300 mM NaCl 0.5 mM EDTA 0.5 mM EGTA 5 mM TCEP. Monomeric actin was labeled at Cys-374 using maleimide conjugated dyes. Dye was incubated with G-actin at a 3-5 fold molar excess for 2 hours at room temperature to achieve a labeling ratio of 20-30%. Unconjugated dye was separated from labeled actin by applying the labeling reaction to a Princeton CentriSpin-20 size exclusion column hydrated with A buffer (5 mM Tris-HCl pH 8, 0.2 mM $CaCl_2$, 0.2 mM ATP, 0.5 mM DTT). The eluted labeled protein was then centrifuged at 14k rpm for 15 min at 4ºC to remove aggregates.

VASP droplet formation and actin polymerization. VASP droplets were formed by mixing VASP with 3% (w/v) PEG-8000 in 50 mM Tris pH 7.4 150 mM NaCl 0.5 mM EDTA 0.5 mM EGTA 5 mM TCEP. PEG was added last to induce droplet formation. All VASP concentrations refer to the concentration of VASP monomer.

For actin polymerization assays within VASP droplets, VASP droplets were formed and labeled monomeric actin was mixed into the droplet solution. An actin to VASP ratio of 1:20 corresponds to 20 uM VASP and 1 uM actin, 1:10 corresponds to 20 uM VASP and 2 uM actin, and 1:7.5 corresponds to 15 uM VASP and 2 uM actin. For end point actin assays (Fig 2a-d, Fig 5), actin was allowed to polymerize in the droplets for 15 minutes, then the droplets were imaged. For phalloidin-actin assays (Fig 3a, c-f), unlabeled actin monomers were added to VASP droplets and allowed to polymerize for 15 minutes. Phalloidin-iFluor488 (Abcam) was added to stain filamentous actin for 15 minutes, then the droplets were imaged. For time lapses of actin polymerization within VASP droplets (Fig 2 e-f, Figs 6 and 7), VASP droplets were prepared in droplet buffer supplemented with oxygen scavengers (130 µg/ml glucose oxidase, 24 µg/ml catalase, and 40 mM glucose), actin was added, and imaging was initiated within 3 minutes. For quantification of growing actin bundles (Figures 6 and 7) droplet buffer without EDTA or EGTA was used, and supplemented with scavengers and 1 mM ATP.

For FRAP (Fig 1f) 15 uM VASP droplets labeled with 3% Atto-488 were formed as above, in droplet buffer supplemented with oxygen scavengers

Microscopy. Samples were prepared in wells formed by 1.5 mm thick silicone gaskets (Grace Biolabs) on Hellmanex II (Hellma) cleaned, no.1.5 glass coverslips (VWR) passivated with PLL-PEG. A second coverslip was placed on top to seal the imaging chamber to prevent evaporation during imaging. Fluorescence microscopy was performed using the Olympus SpinSR10 spinning disc confocal microscope fitted with a Hamamatsu Orca Flash 4.0V3 SCMOS Digital Camera. FRAP was performed using the Olympus FRAP unit 405 nm laser. In some cases, super resolution with deconvolution was performed to better visualize actin filaments within VASP droplets.

PLL-PEG was prepared as described previously with minor alteration [51]. Briefly, amine-reactive mPEG-SVA was conjugated to Poly-L-Lysine (15-30 kD) at a molar ratio of 1:5 PEG to poly-L-lysine. The conjugation reaction was performed in 50 mM sodium

tetraborate pH 8.5 solution and allowed to react overnight at room temperature with continued stirring. The product was buffer exchanged into PBS pH 7.4 using Zeba spin desalting columns (7K MWCO, ThermoFisher) and stored at 4ºC.

Image analysis. ImageJ was used to quantify the distribution of droplet characteristics. Droplets were selected by thresholding in the VASP channel, and shape descriptors (e.g. diameter, aspect ratio) and protein intensities were measured using the analyze particles function. Quantification of actin shapes in droplets was performed by scoring 3 images from each replicate, (n= 3 total replicates) for the presence or absence of uniform actin, rings, ovals, and rods. Uniform droplets were defined as droplets with AR <1.1 that contain uniform actin staining. Rings were defined as droplets with AR < 1.1 that exhibited a decrease in fluorescence intensity in the center of the droplet. Ovals were defined as droplets with AR > 1.1 that exhibited a decrease in fluorescence intensity in the center of the droplet. Rods were defined as droplets with AR > 1.1 that contain uniform actin staining.

Quantification of the ring thickness within the droplets was performed by measuring the phalloidin-actin intensity across a radial line bisecting the ring, and taking the full width at half maximum intensity (with the diffraction limit subtracted). In order to compare droplet diameters among aspherical droplets with AR > 1, we calculated an effective spherical diameter for the droplets based on their major and minor axis lengths: $D = \sqrt[3]{ab^2}$ where a refers to the major axis and b refers to the minor axis lengths. Rings, discs, and shells were differentiated by making 3D projections of each individual droplet. Shells were defined as spherical droplets that have uniform actin intensity in the 3D projection. Rings were defined as spherical droplets that contained a planar arrangement of actin in the 3D projection. Discs were defined as non-spherical, planar droplets that colocalized both actin and VASP. Only droplets with clear peripheral accumulation of actin in the imaging plane were counted.

To calculate the elongation rate of bundles in ImageJ, single droplets were selected by thresholding, and the long axis length was measured over time using the analyze particles function. The change in length per frame (termed “growth”) was then plotted against time, and the slope of the line was used to determine the elongation rate. Only droplets that elongated into straight linear bundles, and persisted for at least 10 frames were counted, ie: bundles that curved, or elongated out of the focal plane were discarded. Bundles that were a product of multiple droplets merging or zippering were also discarded. For bundles that elongated bidirectionally, the droplet was segmented in the middle and the two elongating halves were measured independently.

FRAP data was analyzed using the FRAP Profiler plugin for ImageJ. Fluorescence recovery of a ~2 um diameter region was measured over time, and intensities were normalized to the maximum pre-bleach and minimum post-bleach intensity. All intensity data was corrected for photobleaching. Recovery was measured only for droplets of similar diameters.

Acknowledgements

This research was supported by grants from the National Institutes of Health to JCS (R35GM139531) and PR (R01GM132106), by the National Science Foundation through

a Modulus Grant BIO-1934509 to PR and JCS, and by the Welch Foundation through Grant F-2047 to JCS.

References

1. Hansen, S. D.; Mullins, R. D., VASP is a processive actin polymerase that requires monomeric actin for barbed end association. *J Cell Biol* **2010,** *191* (3), 571-84.

2. Krause, M.; Dent, E. W.; Bear, J. E.; Loureiro, J. J.; Gertler, F. B., Ena/VASP Proteins: Regulators of the Actin Cytoskeleton and Cell Migration. In *Annual Review of Cell and Developmental Biology*, 2003; Vol. 19, pp 541-564.

3. Drees, B.; Friederich, E.; Fradelizi, J.; Louvard, D.; Beckerle, M. C.; Golsteyn, R. M., Characterization of the interaction between zyxin and members of the Ena/vasodilator-stimulated phosphoprotein family of proteins. *Journal of Biological Chemistry* **2000,** *275* (29), 22503-22511.

4. Krause, M.; Leslie, J. D.; Stewart, M.; Lafuente, E. M.; Valderrama, F.; Jagannathan, R.; Strasser, G. A.; Rubinson, D. A.; Liu, H.; Way, M.; Yaffe, M. B.; Boussiotis, V. A.; Gertler, F. B., Lamellipodin, an Ena/VASP ligand, is implicated in the regulation of lamellipodial Dynamics. *Developmental Cell* **2004,** *7* (4), 571-583.

5. Reinhard, M.; Jouvenal, K.; Tripier, D.; Walter, U., Identification, purification, and characterization of a zyxin-related protein that binds the focal adhesion and microfilament protein VASP (vasodilator-stimulated phosphoprotein). *Proceedings of the National Academy of Sciences of the United States of America* **1995,** *92* (17), 7956-7960.

6. Reinhard, M.; Rüdiger, M.; Jockusch, B. M.; Walter, U., VASP interaction with vinculin: A recurring theme of interactions with proline-rich motifs. *FEBS Letters* **1996,** *399* (1-2), 103-107.

7. Disanza, A.; Bisi, S.; Winterhoff, M.; Milanesi, F.; Ushakov, D. S.; Kast, D.; Marighetti, P.; Romet-Lemonne, G.; Muller, H. M.; Nickel, W.; Linkner, J.; Waterschoot, D.; Ampe, C.; Cortellino, S.; Palamidessi, A.; Dominguez, R.; Carlier, M. F.; Faix, J.; Scita, G., CDC42 switches IRSp53 from inhibition of actin growth to elongation by clustering of VASP. *EMBO J* **2013,** *32* (20), 2735-50.

8. Reinhard, M.; Giehl, K.; Abel, K.; Haffner, C.; Jarchau, T.; Hoppe, V.; Jockusch, B. M.; Walter, U., The proline-rich focal adhesion and microfilament protein VASP is a ligand for profilins. *The EMBO Journal* **1995,** *14* (8), 1583-1589.

9. Kuhnel, K.; Jarchau, T.; Wolf, E.; Schlichting, I.; Walter, U.; Wittinghofer, A.; Strelkov, S. V., The VASP tetramerization domain is a right-handed coiled coil based on a 15-residue repeat. *Proceedings of the National Academy of Sciences of the United States of America* **2004,** *101* (49), 17027-32.

10. Bachmann, C.; Fischer, L.; Walter, U.; Reinhard, M., The EVH2 domain of the vasodilator-stimulated phosphoprotein mediates tetramerization, F-actin binding, and actin bundle formation. *J Biol Chem* **1999,** *274* (33), 23549-57.

11. Cheng, K. W.; Mullins, R. D., Initiation and disassembly of filopodia tip complexes containing VASP and lamellipodin. *Mol Biol Cell* **2020,** *31* (18), 2021-2034.

12. Hansen, S. D.; Mullins, R. D., Lamellipodin promotes actin assembly by clustering Ena/VASP proteins and tethering them to actin filaments. *Elife* **2015,** *4*.

13. Bruhmann, S.; Ushakov, D. S.; Winterhoff, M.; Dickinson, R. B.; Curth, U.; Faix, J., Distinct VASP tetramers synergize in the processive elongation of individual actin filaments from clustered arrays. *Proceedings of the National Academy of Sciences of the United States of America* **2017,** *114* (29), E5815-E5824.

14. Breitsprecher, D.; Kiesewetter, A. K.; Linkner, J.; Urbanke, C.; Resch, G. P.; Small, J. V.; Faix, J., Clustering of VASP actively drives processive, WH2 domain-mediated actin filament elongation. *EMBO J* **2008,** *27* (22), 2943-54.

15. Brangwynne, Clifford P.; Tompa, P.; Pappu, Rohit V., Polymer physics of intracellular phase transitions. *Nature Physics* **2015,** *11*, 899.

16. Li, P.; Banjade, S.; Cheng, H. C.; Kim, S.; Chen, B.; Guo, L.; Llaguno, M.; Hollingsworth, J. V.; King, D. S.; Banani, S. F.; Russo, P. S.; Jiang, Q. X.; Nixon, B. T.; Rosen, M. K., Phase transitions in the assembly of multivalent signalling proteins. *Nature* **2012,** *483* (7389), 336-40.

17. Banani, S. F.; Rice, A. M.; Peeples, W. B.; Lin, Y.; Jain, S.; Parker, R.; Rosen, M. K., Compositional Control of Phase-Separated Cellular Bodies. *Cell* **2016,** *166* (3), 651-663.

18. Lancaster, A. K.; Nutter-Upham, A.; Lindquist, S.; King, O. D., PLAAC: a web and command-line application to identify proteins with prion-like amino acid composition. *Bioinformatics* **2014,** *30* (17), 2501-2.

19. Woodruff, J. B.; Ferreira Gomes, B.; Widlund, P. O.; Mahamid, J.; Honigmann, A.; Hyman, A. A., The Centrosome Is a Selective Condensate that Nucleates Microtubules by Concentrating Tubulin. *Cell* **2017,** *169* (6), 1066-1077 e10.

20. Banjade, S.; Rosen, M. K., Phase transitions of multivalent proteins can promote clustering of membrane receptors. *Elife* **2014,** *3*.

21. Drozdetskiy, A.; Cole, C.; Procter, J.; Barton, G. J., JPred4: a protein secondary structure prediction server. *Nucleic Acids Res* **2015,** *43* (W1), W389-94.

22. Oates, M. E.; Romero, P.; Ishida, T.; Ghalwash, M.; Mizianty, M. J.; Xue, B.; Dosztanyi, Z.; Uversky, V. N.; Obradovic, Z.; Kurgan, L.; Dunker, A. K.; Gough, J., D(2)P(2): database of disordered protein predictions. *Nucleic Acids Res* **2013,** *41* (Database issue), D508-16.

23. Ball, L. J.; Jarchau, T.; Oschkinat, H.; Walter, U., EVH1 domains: structure, function and interactions. *FEBS Lett* **2002,** *513* (1), 45-52.

24. Ambadipudi, S.; Biernat, J.; Riedel, D.; Mandelkow, E.; Zweckstetter, M., Liquid–liquid phase separation of the microtubule-binding repeats of the Alzheimer-related protein Tau. *Nature Communications 2017 8:1* **2017,** *8* (1), 1-13.

25. Mitrea, D. M.; Cika, J. A.; Stanley, C. B.; Nourse, A.; Onuchic, P. L.; Banerjee, P. R.; Phillips, A. H.; Park, C. G.; Deniz, A. A.; Kriwacki, R. W., Self-interaction of NPM1 modulates multiple mechanisms of liquid–liquid phase separation. *Nature Communications 2018 9:1* **2018,** *9* (1), 1-13.

26. Molliex, A.; Temirov, J.; Lee, J.; Coughlin, M.; Kanagaraj, A. P.; Kim, H. J.; Mittag, T.; Taylor, J. P., Phase Separation by Low Complexity Domains Promotes Stress Granule Assembly and Drives Pathological Fibrillization. *Cell* **2015,** *163* (1), 123-133.

27. Uversky, V. N., Intrinsically Disordered Proteins and Their Environment: Effects of Strong Denaturants, Temperature, pH, Counter Ions, Membranes, Binding Partners, Osmolytes, and Macromolecular Crowding. *The Protein Journal 2009 28:7* **2009,** *28* (7), 305-325.

28. Alberti, S.; Gladfelter, A.; Mittag, T., Considerations and Challenges in Studying Liquid-Liquid Phase Separation and Biomolecular Condensates. *Cell* **2019,** *176* (3), 419-434.

29. Nakashima, K. K.; Vibhute, M. A.; Spruijt, E., Biomolecular Chemistry in Liquid Phase Separated Compartments. *Front Mol Biosci* **2019,** *6*, 21.

30. Elbaum-Garfinkle, S.; Kim, Y.; Szczepaniak, K.; Chen, C. C.; Eckmann, C. R.; Myong, S.; Brangwynne, C. P., The disordered P granule protein LAF-1 drives phase separation into droplets with tunable viscosity and dynamics. *Proceedings of the National Academy of Sciences of the United States of America* **2015,** *112* (23), 7189-94.

31. Carl, U. D.; Pollmann, M.; Orr, E.; Gertler, F. B.; Chakraborty, T.; Wehland, J., Aromatic and basic residues within the EVH1 domain of VASP specify its interaction with proline-rich ligands. *Current Biology* **1999,** *9* (13), 715-718.

32. Limozin, L.; Barmann, M.; Sackmann, E., On the organization of self-assembled actin networks in giant vesicles. *Eur Phys J E Soft Matter* **2003,** *10* (4), 319-30.

33. Miyazaki, M.; Chiba, M.; Eguchi, H.; Ohki, T.; Ishiwata, S., Cell-sized spherical confinement induces the spontaneous formation of contractile actomyosin rings in vitro. *Nat Cell Biol* **2015,** *17* (4), 480-9.

34. Cohen, A. E.; Mahadevan, L., Kinks, rings, and rackets in filamentous structures. *Proceedings of the National Academy of Sciences of the United States of America* **2003,** *100* (21), 12141-6.

35. Limozin, L.; Sackmann, E., Polymorphism of Cross-Linked Actin Networks in Giant Vesicles. *Physical Review Letters* **2002,** *89* (16), 168103.

36. Claessens, M. M. A. E.; Tharmann, R.; Kroy, K.; Bausch, A. R., Microstructure and viscoelasticity of confined semiflexible polymer networks. *Nature Physics* **2006,** *2* (3), 186-189.

37. Mattila, P. K.; Lappalainen, P., Filopodia: molecular architecture and cellular functions. *Nat Rev Mol Cell Biol* **2008,** *9* (6), 446-54.

38. Kassianidou, E.; Kumar, S., A biomechanical perspective on stress fiber structure and function. *Biochim Biophys Acta* **2015,** *1853* (11 Pt B), 3065-74.

39. Breitsprecher, D.; Kiesewetter, A. K.; Linkner, J.; Vinzenz, M.; Stradal, T. E. B.; Small, J. V.; Curth, U.; Dickinson, R. B.; Faix, J., Molecular mechanism of Ena/VASP-mediated actin-filament elongation. *EMBO Journal* **2011,** *30* (3), 456-467.

40. Bornschlogl, T.; Romero, S.; Vestergaard, C. L.; Joanny, J. F.; Nhieu, G. T. V.; Bassereau, P., Filopodial retraction force is generated by cortical actin dynamics and controlled by reversible tethering at the tip. *Proceedings of the National Academy of Sciences of the United States of America* **2013,** *110* (47), 18928-18933.

41. Applewhite, D. A.; Barzik, M.; Kojima, S. I.; Svitkina, T. M.; Gertler, F. B.; Borisy, G. G., Ena/VASP proteins have an anti-capping independent function in filopodia formation. *Molecular Biology of the Cell* **2007,** *18* (7), 2579-2591.

42. McCall, P. M.; Srivastava, S.; Perry, S. L.; Kovar, D. R.; Gardel, M. L.; Tirrell, M. V., Partitioning and Enhanced Self-Assembly of Actin in Polypeptide Coacervates. *Biophys J* **2018,** *114* (7), 1636-1645.

43. Scheff, D. R.; Weirich, K. L.; Dasbiswas, K.; Patel, A.; Vaikuntanathan, S.; Gardel, M. L., Tuning shape and internal structure of protein droplets via biopolymer filaments. *Soft Matter* **2020,** *16* (24), 5659-5668.

44. Hernandez-Vega, A.; Braun, M.; Scharrel, L.; Jahnel, M.; Wegmann, S.; Hyman, B. T.; Alberti, S.; Diez, S.; Hyman, A. A., Local Nucleation of Microtubule Bundles through Tubulin Concentration into a Condensed Tau Phase. *Cell Rep* **2017,** *20* (10), 2304-2312.

45. Gittes, F.; Mickey, B.; Nettleton, J.; Howard, J., Flexural rigidity of microtubules and actin filaments measured from thermal fluctuations in shape. *J Cell Biol* **1993,** *120* (4), 923-34.

46. Krause, M.; Dent, E. W.; Bear, J. E.; Loureiro, J. J.; Gertler, F. B., Ena/VASP Proteins: Regulators of the Actin Cytoskeleton and Cell Migration. *Annual Review of Cell and Developmental Biology* **2003,** *19*, 541-564.

47. Blanchoin, L.; Boujemaa-Paterski, R.; Sykes, C.; Plastino, J., Actin Dynamics, Architecture, and Mechanics in Cell Motility. *Physiological Reviews* **2014,** *94* (1), 235-263.

48. Case, L. A.-O.; De Pasquale, M.; Henry, L.; Rosen, M. A.-O., Synergistic phase separation of two pathways promotes integrin clustering and nascent adhesion formation. LID - 10.7554/eLife.72588 [doi] LID - e72588. (2050-084X (Electronic)).

49. Legerstee, K.; Geverts, B.; Slotman, J. A.; Houtsmuller, A. B., Dynamics and distribution of paxillin, vinculin, zyxin and VASP depend on focal adhesion location and orientation. *Scientific Reports* **2019,** *9* (1), 10460.

50. Wang, Y.; Zhang, C.; Yang, W.; Shao, S.; Xu, X.; Sun, Y.; Li, P.; Liang, L.; Wu, C., LIMD1 phase separation contributes to cellular mechanics and durotaxis by regulating focal adhesion dynamics in response to force. *Developmental Cell* **2021,** *56* (9), 1313-1325.e7.

51. Zeno, W. F.; Baul, U.; Snead, W. T.; DeGroot, A. C. M.; Wang, L.; Lafer, E. M.; Thirumalai, D.; Stachowiak, J. C., Synergy between intrinsically disordered domains and structured proteins amplifies membrane curvature sensing. *Nature Communications* **2018,** *9* (1), 4152.